Supplementary Information

Realizing altermagnetism in two-dimensional metal-organic framework semiconductor with electric-field-controlled anisotropic spin current

Yixuan Che,[1] Haifeng Lv,[*b] Xiaojun Wu[*ab] and Jinlong Yang[ab]

[a] Hefei National Research Center for Physical Sciences at the Microscale, University of Science and Technology of China, Hefei, Anhui 230026, China
[b] Key Laboratory of Precision and Intelligent Chemistry, CAS Key Laboratory of Materials for Energy Conversion, School of Chemistry and Materials Science, and Collaborative Innovation Center of Chemistry for Energy Materials (iChEM), University of Science and Technology of China, Hefei, Anhui 230026, China

[*] E-mail(s): hflv@ustc.edu.cn (H.L.); xjwu@ustc.edu.cn (X.W.)

CONTENTS

NOTES

Note S1. Spin point group representations.

The theory of spin groups in crystals was first proposed by Litvin and Opechowski in 1974,[1] and the 598 classes of nontrivial spin point groups were derived and tabulated in 1977.[2] Considering the element $[R_i||R_j]$, the left component of the double vertical bar R_i affects only the spin space ($\mathbb{B}$) while the right component R_j affects only the crystalline real space ($\mathbb{R}$).

The spin point group ($\mathbf{R}_s$) can be derived as

$$\mathbf{R}_s = [E||\mathbf{r}] + [B_2||R_2][E||\mathbf{r}] + \cdots + [B_n||R_n][E||\mathbf{r}], \tag{S1}$$

where $\mathbf{r}$ represents a normal subgroup of a specific crystallographic point group $\mathbf{R}$, and the notation of ${}^{B}R$ in the spin point groups represents the element $[B||R]$. Taking the altermagnetic KRu_4O_8 as an example,[3] the spin point group can be defined as

$$\mathbf{R}_s = [E||2/m] + [C_2||C_{4z}][E||2/m]. \tag{S2}$$

Since $\mathbf{R} = 4/m$, and $[C_2||C_{4z}]$ and $[E||2/m]$ are elements of $\mathbf{R}_s$, the spin point group of KRu_4O_8 is denoted by ${}^{2}4/{}^{1}m$.

The spin point group representations of different types of magnetism were summarized by Šmejkal *et al.* in 2022 as below.[3]

$$\mathbf{R}_s^{\mathrm{I}} = [E||\mathbf{G}], \text{ for ferromagnets and ferrimagnets;} \tag{S3a}$$

$$\mathbf{R}_s^{\mathrm{II}} = [E||\mathbf{G}] + [C_2||\mathbf{G}], \text{ for conventional antiferromagnets;} \tag{S3b}$$

$$\mathbf{R}_s^{\mathrm{III}} = [E||\mathbf{H}] + [C_2||A][E||\mathbf{H}] = [E||\mathbf{H}] + [C_2||\mathbf{G} \ominus \mathbf{H}], \text{ for altermagnets.} \tag{S3c}$$

In **Eq. S3c**, $\mathbf{H}$ is a halving subgroup of the crystallographic Laue group $\mathbf{G}$ and the coset $\mathbf{G} \ominus \mathbf{H} = A\mathbf{H}$ is generated by transformations A that can be only real-space rotations (R) and cannot be translation (t) or inversion (i).

The spin point group representations can provide a good explanation for the band structrues to different types of magnetism as follows.

(1) For ferromagnets and ferrimagnets (**Eq. S3a**), $\mathbf{R}_s$ do not imply spin degeneracy of $\mathcal{E}(s,\mathbf{k})$ at any k-point, thus describing the spin-splitting with broken time-reversal ($\mathcal{T}$) symmetry and nonzero macroscopic magnetization. Note that the notation $\mathcal{E}(s,\mathbf{k})$ represents the spin (s) and crystal momenta ($\mathbf{k}$) dependent energy isosurfaces ($\mathcal{E}$).

(2) For conventional antiferromagnets (**Eq. S3b**), due to the real space identity E is contained in $\mathbf{G}$, the $[C_2||E]$ symmetry in $\mathbf{R}_s$ results in the spin degeneracy $\mathcal{E}(s,\mathbf{k})$ for all k-vectors in the Brillouin zone, indicating the spin-degenerate band structures with $\mathcal{T}$ invariance and a macroscopic zero magnetization.

(3) For altermagnets in this work (**Eq. S3c**), the representation of $\mathbf{R}_s$ corresponds to the crystal structure in which the sublattices with opposite spins are connected by rotation and not by translation or inversion, and the real space inversion in $\mathbf{G}$ is always contained in $\mathbf{H}$. The coset $\mathbf{G} \ominus \mathbf{H}$ does not contain E, thus the spin groups of altermagnets do not contain the $\mathcal{T}$-symmetry element, and the lifted spin degeneracies in $\mathbf{R}_s$ are allowed for $\mathbf{k}$ with $A\mathbf{H}\mathbf{k} = \mathbf{k}' \neq \mathbf{k}$ and

$$\mathcal{E}(s,\mathbf{k}) = [C_2||A\mathbf{H}]\mathcal{E}(s,\mathbf{k}) = \mathcal{E}(-s,\mathbf{k}'). \tag{S4}$$

indicating that the energy isosurfaces of different spins are split but with the same number of states. Thus, altermagnets show a macroscopic zero magnetization with partial spin-splitting.

Note S2. Anisotropic spin conductivity.

Under a general electric field, the conductivity of a semiconductor follows Ohm's law, *i.e.* $\boldsymbol{J} = \sigma \boldsymbol{E}$, thus the anisotropy of spin current can be represented by conductivity. The direct current conductivity tensor ($\boldsymbol{\sigma}_{ij}$) for an anisotropic 2D material can be derived from Boltzmann transport equation as[4]

$$\boldsymbol{\sigma}_{ij} = \sum_n \left[e^2 \tau \int \frac{\mathrm{d}^2 k}{4\pi^2} f\left(\mathcal{E}_n(\mathbf{k})\right) \frac{1}{\hbar^2} \frac{\partial^2 \mathcal{E}_n(\mathbf{k})}{\partial k_i \partial k_j} \right], \tag{S5}$$

where $i, j = x$ or y, and n and $\mathcal{E}_n(\mathbf{k})$ represents the band index and energy, respectively. The relaxation time τ can be taken as a constant under a steady state of constant $\boldsymbol{E}$ and f is the Fermi-Dirac distribution function

$$f(\mathcal{E}) = \frac{1}{\exp\left\{\dfrac{\mathcal{E} - \mathcal{E}_\mathrm{F}}{k_B T}\right\} + 1}. \tag{S6}$$

Since the rotation of the pyrazine ligands is around the ⟨110⟩ direction of the 3D real space with the same angle, the symmetries of sublattices on the (001) surface with the same spin are the same. Therefore, for the sake of simplicity, we can select the k_x-axis in the direction of a certain arrangement of sublattices with the same spin at the level of 2D spin space, as shown in the illustration below.

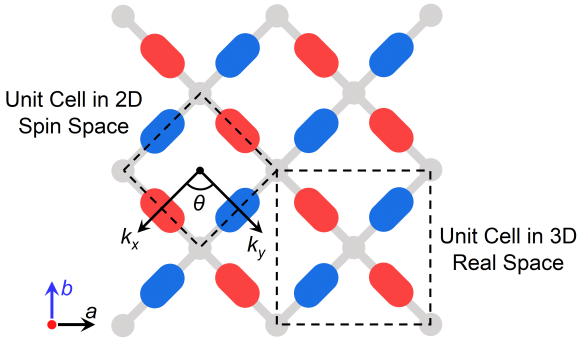

The energy of the spin valley along the k_x-axis (α) can be written as

$$\mathcal{E}_\alpha = \frac{\hbar^2}{2m_1} k_x^2 + \frac{\hbar^2}{2m_2} k_y^2. \tag{S7}$$

For another valley β which is related with α by a rotation operation $\boldsymbol{C}_n$, where $n = \dfrac{2\pi}{\theta}$ is the axis order with the angle of θ, defining $\beta = \boldsymbol{C}_n \alpha$, the k_x' and k_y' for β can be derived by

$$\begin{bmatrix} k_x' \\ k_y' \end{bmatrix} = \boldsymbol{C}_n^{-1} \begin{bmatrix} k_x \\ k_y \end{bmatrix} = \begin{bmatrix} \cos\theta & \sin\theta \\ -\sin\theta & \cos\theta \end{bmatrix} \begin{bmatrix} k_x \\ k_y \end{bmatrix}. \tag{S8}$$

Thus,

$$\mathcal{E}_\beta = \frac{\hbar^2}{2m_1} k_x'^2 + \frac{\hbar^2}{2m_2} k_y'^2 = \frac{\hbar^2}{2m_1} \left(k_x \cos\theta + k_y \sin\theta\right)^2 + \frac{\hbar^2}{2m_2} \left(-k_x \sin\theta + k_y \cos\theta\right)^2. \tag{S9}$$

Based on **Eq. S5**, $f(\mathcal{E}) = 1$ when $T = 0$ K, and the conductivity can be written as

$$\sigma = \frac{n e^2 \tau}{m^*}, \tag{S10}$$

which can also be derived from the classic Sommerfeld's free electron theory. Here, n is the carrier density, and $m^* = \dfrac{\hbar^2}{\mathrm{d}^2\mathcal{E}/\mathrm{d}k^2}$ is the effective mass. For an anisotropic 2D material, m^* is usually presented in the form of a reciprocal tensor

$$\left[\frac{1}{m^*}\right] = \frac{1}{\hbar^2}\begin{bmatrix} \dfrac{\partial^2\mathcal{E}}{\partial k_x^2} & \dfrac{\partial^2\mathcal{E}}{\partial k_x \partial k_y} \\ \dfrac{\partial^2\mathcal{E}}{\partial k_y \partial k_x} & \dfrac{\partial^2\mathcal{E}}{\partial k_y^2} \end{bmatrix}. \tag{S11}$$

For an electric field $\boldsymbol{E}$ with a direction of an angle φ from the k_x-axis as shown in the illustration below, the contributions of k_x and k_y to the direction along (k_x'') and perpendicular (k_y'') to $\boldsymbol{E}$ can also be written as

$$\begin{bmatrix} k_x'' \\ k_y'' \end{bmatrix} = \begin{bmatrix} \cos\varphi & \sin\varphi \\ -\sin\varphi & \cos\varphi \end{bmatrix}\begin{bmatrix} k_x \\ k_y \end{bmatrix}. \tag{S12}$$

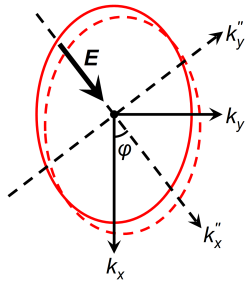

The solution of effective mass should be transferred to the $k_x''Ok_y''$ plane rectangular coordinate system, *i.e.*, k_x and k_y in **Eq. S11** are transformed into k_x'' and k_y'', respectively. Thus, $\mathcal{E}_\alpha$ and $\mathcal{E}_\beta$ in **Eqs. S7** and **S9** will be derived as

$$\begin{aligned}
\mathcal{E}_\alpha &= \begin{bmatrix} k_x & k_y \end{bmatrix}\begin{bmatrix} \dfrac{\hbar^2}{2m_1} & 0 \\ 0 & \dfrac{\hbar^2}{2m_2} \end{bmatrix}\begin{bmatrix} k_x \\ k_y \end{bmatrix} \\
&= \begin{bmatrix} k_x'' & k_y'' \end{bmatrix}\begin{bmatrix} \cos\varphi & -\sin\varphi \\ \sin\varphi & \cos\varphi \end{bmatrix}^{-1}\begin{bmatrix} \dfrac{\hbar^2}{2m_1} & 0 \\ 0 & \dfrac{\hbar^2}{2m_2} \end{bmatrix}\begin{bmatrix} \cos\varphi & \sin\varphi \\ -\sin\varphi & \cos\varphi \end{bmatrix}^{-1}\begin{bmatrix} k_x'' \\ k_y'' \end{bmatrix} \\
&= \begin{bmatrix} k_x'' & k_y'' \end{bmatrix}\begin{bmatrix} \cos\varphi & \sin\varphi \\ -\sin\varphi & \cos\varphi \end{bmatrix}\begin{bmatrix} \dfrac{\hbar^2}{2m_1} & 0 \\ 0 & \dfrac{\hbar^2}{2m_2} \end{bmatrix}\begin{bmatrix} \cos\varphi & -\sin\varphi \\ \sin\varphi & \cos\varphi \end{bmatrix}\begin{bmatrix} k_x'' \\ k_y'' \end{bmatrix} \\
&= \begin{bmatrix} k_x''\cos\varphi - k_y''\sin\varphi & k_x''\sin\varphi + k_y''\cos\varphi \end{bmatrix}\begin{bmatrix} \dfrac{\hbar^2}{2m_1} & 0 \\ 0 & \dfrac{\hbar^2}{2m_2} \end{bmatrix}\begin{bmatrix} k_x''\cos\varphi - k_y''\sin\varphi \\ k_x''\sin\varphi + k_y''\cos\varphi \end{bmatrix} \\
&= \frac{\hbar^2}{2m_1}\left(k_x''\cos\varphi - k_y''\sin\varphi\right)^2 + \frac{\hbar^2}{2m_2}\left(k_x''\sin\varphi + k_y''\cos\varphi\right)^2
\end{aligned} \tag{S13}$$

and

$$\begin{aligned}
\mathcal{E}_\beta &= \begin{bmatrix} k_x' & k_y' \end{bmatrix} \begin{bmatrix} \frac{\hbar^2}{2m_1} & 0 \\ 0 & \frac{\hbar^2}{2m_2} \end{bmatrix} \begin{bmatrix} k_x' \\ k_y' \end{bmatrix} \\
&= \begin{bmatrix} k_x'' & k_y'' \end{bmatrix} \begin{bmatrix} \cos\varphi & \sin\varphi \\ -\sin\varphi & \cos\varphi \end{bmatrix} \begin{bmatrix} \cos\theta & -\sin\theta \\ \sin\theta & \cos\theta \end{bmatrix} \begin{bmatrix} \frac{\hbar^2}{2m_1} & 0 \\ 0 & \frac{\hbar^2}{2m_2} \end{bmatrix} \begin{bmatrix} \cos\theta & \sin\theta \\ -\sin\theta & \cos\theta \end{bmatrix} \begin{bmatrix} \cos\varphi & -\sin\varphi \\ \sin\varphi & \cos\varphi \end{bmatrix} \begin{bmatrix} k_x'' \\ k_y'' \end{bmatrix} \\
&= \begin{bmatrix} k_x'' & k_y'' \end{bmatrix} \begin{bmatrix} \cos(\varphi-\theta) & \sin(\varphi-\theta) \\ -\sin(\varphi-\theta) & \cos(\varphi-\theta) \end{bmatrix} \begin{bmatrix} \frac{\hbar^2}{2m_1} & 0 \\ 0 & \frac{\hbar^2}{2m_2} \end{bmatrix} \begin{bmatrix} \cos(\varphi-\theta) & -\sin(\varphi-\theta) \\ \sin(\varphi-\theta) & \cos(\varphi-\theta) \end{bmatrix} \begin{bmatrix} k_x'' \\ k_y'' \end{bmatrix} \\
&= \frac{\hbar^2}{2m_1}\left[k_x''\cos(\varphi-\theta) - k_y''\sin(\varphi-\theta)\right]^2 + \frac{\hbar^2}{2m_2}\left[k_x''\sin(\varphi-\theta) + k_y''\cos(\varphi-\theta)\right]^2, \qquad \text{(S14)}
\end{aligned}$$

respectively. The $\boldsymbol{\sigma}$ tensors of α and β spins at 0 K can be then derived from the second-order partial derivative of $\mathcal{E}$ from **Eq. S11**, *i.e.*,

$$\boldsymbol{\sigma}_\alpha = \frac{ne^2\tau}{m_1 m_2} \begin{bmatrix} m_1\sin^2\varphi + m_2\cos^2\varphi & \frac{1}{2}(m_1-m_2)\sin(2\varphi) \\ \frac{1}{2}(m_1-m_2)\sin(2\varphi) & m_1\cos^2\varphi + m_2\sin^2\varphi \end{bmatrix} \qquad \text{(S15)}$$

and

$$\boldsymbol{\sigma}_\beta = \frac{ne^2\tau}{m_1 m_2} \begin{bmatrix} m_1\sin^2(\varphi-\theta) + m_2\cos^2(\varphi-\theta) & \frac{1}{2}(m_1-m_2)\sin(2\varphi-2\theta) \\ \frac{1}{2}(m_1-m_2)\sin(2\varphi-2\theta) & m_1\cos^2(\varphi-\theta) + m_2\sin^2(\varphi-\theta) \end{bmatrix}. \qquad \text{(S16)}$$

The diagonal and off-diagonal elements refer to the longitudinal and transverse (or Hall) part of the conductivity. Thus, the charge ($\boldsymbol{\sigma}$) and spin ($\boldsymbol{\sigma}_s$) conductivities are

$$\boldsymbol{\sigma} = \boldsymbol{\sigma}_\alpha + \boldsymbol{\sigma}_\beta = \frac{ne^2\tau}{m_1 m_2} \begin{bmatrix} m_1\psi_1(\varphi,\theta) + m_2\psi_2(\varphi,\theta) & (m_1-m_2)\cos\theta\sin(2\varphi-\theta) \\ (m_1-m_2)\cos\theta\sin(2\varphi-\theta) & m_1\psi_2(\varphi,\theta) + m_2\psi_1(\varphi,\theta) \end{bmatrix} \qquad \text{(S17)}$$

and

$$\boldsymbol{\sigma}_s = \boldsymbol{\sigma}_\alpha - \boldsymbol{\sigma}_\beta = \frac{ne^2\tau}{m_1 m_2} \begin{bmatrix} (m_1-m_2)\sin\theta\sin(2\varphi-\theta) & (m_1-m_2)\sin\theta\cos(2\varphi-\theta) \\ (m_1-m_2)\sin\theta\cos(2\varphi-\theta) & -(m_1-m_2)\sin\theta\sin(2\varphi-\theta) \end{bmatrix}, \qquad \text{(S18)}$$

where $\psi_1 = \sin^2\varphi + \sin^2(\varphi-\theta)$ and $\psi_2 = \cos^2\varphi + \cos^2(\varphi-\theta)$. The charge-spin conversion ratio (δ) can be then defined as

$$\delta(\theta,\varphi) = \left|\frac{\sigma_{s,xy}}{\sigma_{xx}}\right| = \left|\frac{(m_1-m_2)\sin\theta\cos(2\varphi-\theta)}{m_1\left[\sin^2\varphi + \sin^2(\varphi-\theta)\right] + m_2\left[\cos^2\varphi + \cos^2(\varphi-\theta)\right]}\right|. \qquad \text{(S19)}$$

Particularly, when $\boldsymbol{E}$ is just along the angular bisector of α and β spins, *i.e.*, $\varphi = \frac{\theta}{2}$,

$$\boldsymbol{\sigma} = \frac{ne^2\tau}{m_1 m_2} \begin{bmatrix} (m_1+m_2) - (m_1-m_2)\cos\theta & 0 \\ 0 & (m_1+m_2) - (m_1-m_2)\cos\theta \end{bmatrix}, \qquad \text{(S20)}$$

$$\boldsymbol{\sigma}_s = \frac{ne^2\tau}{m_1 m_2}\begin{bmatrix} 0 & (m_1 - m_2)\sin\theta \\ (m_1 - m_2)\sin\theta & 0 \end{bmatrix}, \tag{S21}$$

and

$$\delta(\theta) = \left|\frac{(m_1 - m_2)\sin\theta}{(m_1 + m_2) - (m_1 - m_2)\cos\theta}\right|. \tag{S22}$$

It can be seen that for $\varphi = \frac{\theta}{2}$, the transverse spin current is pure and there is no charge Hall current.

Additionally, we discuss the difference of charge and spin conductivities for antiferromagnets and altermagnets, both of which show a macroscopic zero magnetization. The key is the effective mass from different k-directions. Unlike alermagnets, m_1 is always equal to m_2 in antiferromagnetic materials as shown in the illustration below, thus the off-diagonal elements in **Eqs. S15** and **S16** is always zero, and there is no $\boldsymbol{\sigma}_s$. Note that spin-orbit coupling (SOC) has not taken into account in any of the above results.

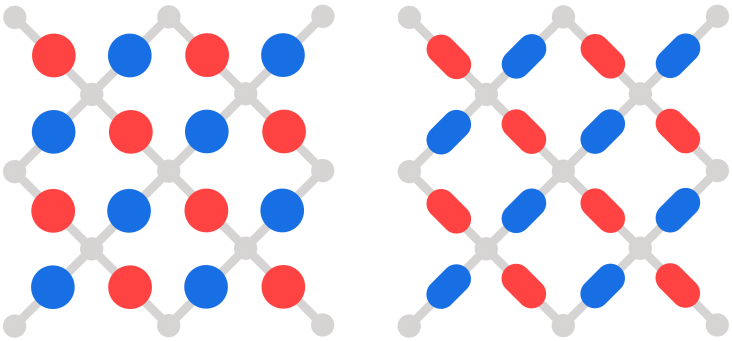

Now we can substitute the derived results into M(pyz)$_2$ (M = Ca and Sr). The sublattices are connected with C_{4z} rotation, *i.e.*, $\theta = \frac{\pi}{2}$. Thus, the band energy of α and β spins at 2D level are

$$\mathcal{E}_\alpha = \frac{\hbar^2}{2m_1}k_x^2 + \frac{\hbar^2}{2m_2}k_y^2 \tag{S23}$$

and

$$\mathcal{E}_\beta = \frac{\hbar^2}{2m_1}k_y^2 + \frac{\hbar^2}{2m_2}k_x^2, \tag{S24}$$

respectively. And the conductivity tensors contributed from two spins at 0 K for $\boldsymbol{E}$ with a direction of an angle φ from the k_x-axis are

$$\boldsymbol{\sigma}_\alpha(\varphi) = \frac{ne^2\tau}{m_1 m_2}\begin{bmatrix} m_1\sin^2\varphi + m_2\cos^2\varphi & \frac{1}{2}(m_1 - m_2)\sin(2\varphi) \\ \frac{1}{2}(m_1 - m_2)\sin(2\varphi) & m_1\cos^2\varphi + m_2\sin^2\varphi \end{bmatrix} \tag{S25}$$

and

$$\boldsymbol{\sigma}_\beta(\varphi) = \frac{ne^2\tau}{m_1 m_2}\begin{bmatrix} m_1\cos^2\varphi + m_2\sin^2\varphi & -\frac{1}{2}(m_1 - m_2)\sin(2\varphi) \\ -\frac{1}{2}(m_1 - m_2)\sin(2\varphi) & m_1\sin^2\varphi + m_2\cos^2\varphi \end{bmatrix}. \tag{S26}$$

Thus, the charge and spin conductivities and the charge-spin conversion ratio are

$$\boldsymbol{\sigma} = \boldsymbol{\sigma}_\alpha + \boldsymbol{\sigma}_\beta = \frac{ne^2\tau}{m_1 m_2}\begin{bmatrix} m_1 + m_2 & 0 \\ 0 & m_1 + m_2 \end{bmatrix}, \tag{S27}$$

$$\boldsymbol{\sigma}_s(\varphi) = \boldsymbol{\sigma}_\alpha - \boldsymbol{\sigma}_\beta = \frac{ne^2\tau}{m_1 m_2}\begin{bmatrix} -(m_1 - m_2)\cos(2\varphi) & (m_1 - m_2)\sin(2\varphi) \\ (m_1 - m_2)\sin(2\varphi) & (m_1 - m_2)\cos(2\varphi) \end{bmatrix}, \tag{S28}$$

and

$$\delta(\varphi) = \left|\frac{\sigma_{s,xy}}{\sigma_{xx}}\right| = \left|\frac{m_1 - m_2}{m_1 + m_2}\sin(2\varphi)\right|. \tag{S29}$$

The altermagnetic 2D M(pyz)$_2$ (M = Ca and Sr) is anisotropic, thus $m_1 \neq m_2$, and $\delta \not\equiv 0$ is a function of φ. Particularly, when $\varphi = \frac{\pi}{4}$, the transverse spin current is pure with no Hall charge current since

$$\boldsymbol{\sigma}_s(\varphi = \frac{\pi}{4}) = \boldsymbol{\sigma}_\alpha - \boldsymbol{\sigma}_\beta = \frac{ne^2\tau}{m_1 m_2}\begin{bmatrix} 0 & m_1 - m_2 \\ m_1 - m_2 & 0 \end{bmatrix}, \tag{S30}$$

and the charge-spin conversion ratio is the largest with the value of

$$\delta(\varphi = \frac{\pi}{4}) = \left|\frac{\sigma_{s,xy}}{\sigma_{xx}}\right| = \left|\frac{m_1 - m_2}{m_1 + m_2}\right|. \tag{S31}$$

Based on **Eq. S4**, the energy isosurfaces of different spins in altermagnetic 2D M(pyz)$_2$ (M = Ca and Sr) are split but with the same number of states. Thus, m^*_{xx} at α valley is equal to m^*_{yy} at β valley, and m^*_{yy} at α valley is equal to m^*_{xx} at β valley. According to **Eqs. S23** and **S24**, the energy isosurface is a quadratic function of k-point coordinates. Therefore, taking the HSE06 band structure at CBM of Ca(pyz)$_2$ as an example (**Fig. 2f**), two curves can be obtained by interpolating from M towards the Σ' and Σ directions (**Fig. S23**). Here, each curve is fitted using a total of nine points, and the spins on the two sides of the stationary point (which is also the vertex) of the curve are opposite.

Fitted by the quadratic function $y = Ax^2 + Bx + C$, where y and x are the energy isosurface and k-point coordination, respectively, the effective masses of k_x and k_y directions can be derived from the second derivative of y, *i.e.*, m^* can be represented by the value of A. As shown in **Fig. S23a**, the A values of two curves are 1.2252 ($R^2_{\text{adj}} = 0.9974$) and 0.3371 ($R^2_{\text{adj}} = 0.9986$), respectively. Thus,

$$\frac{m_1}{m_2} = \frac{1/1.2252}{1/0.3371} = \frac{1}{3.6345}, \tag{S32}$$

and the maximal value of δ at $\varphi = \frac{\pi}{4}$ is $\delta_{\max} = 0.5685$, which corresponds to the angle between the two types of spin transport channels of 59.24° [= 2 × arctan(0.5685)] for Ca(pyz)$_2$. For Sr(pyz)$_2$ (**Fig. S23b**), $\frac{m_1}{m_2} = \frac{1}{13.3291}$ [$R^2_{\text{adj}}(m_1) = 0.9978$, $R^2_{\text{adj}}(m_2) > 0.9999$] and $\delta_{\max} = 0.8604$, corresponding to the angle of 84.42°.

The spin Hall conductivity (SHC, $\sigma^{\text{spin}z}_{xy}$) can be calculated with Kubo formula[5]

$$\sigma^{\text{spin}z}_{xy} = \hbar \int_{\text{BZ}} \frac{\mathrm{d}^3 k}{(2\pi)^3} \sum_n f_{n\mathbf{k}} \sum_{m \neq n} \frac{2\text{Im}[\langle n\mathbf{k}|\hat{j}^{\text{spin}z}_x|m\mathbf{k}\rangle\langle m\mathbf{k}| - e\hat{v_y}|m\mathbf{k}\rangle]}{(\epsilon_{n\mathbf{k}} - \epsilon_{m\mathbf{k}})^2 - (\hbar\omega + \mathrm{i}\eta)^2}, \tag{S33}$$

where n and m are band indexes, ϵ_n and ϵ_m are eigenvalues, $f_{n\mathbf{k}}$ is the Fermi-Dirac distribution function, $\hat{j}^{\text{spin}z}_x = \frac{1}{2}\{\hat{S}_z, \hat{v}_x\}$ is the spin current operator where $\hat{S}_z = \frac{\hbar}{2}\hat{\sigma}_z$, $\hat{v}_y = \frac{1}{\hbar}\frac{\partial \mathcal{H}(\mathbf{k})}{\partial k_y}$ is the velocity operator, and ω and η are frequencies. Here, x and y denote Cartesian directions and z denotes the direction of spin which is obtained from the calculations with SOC (**Table S7**).

FIGURES

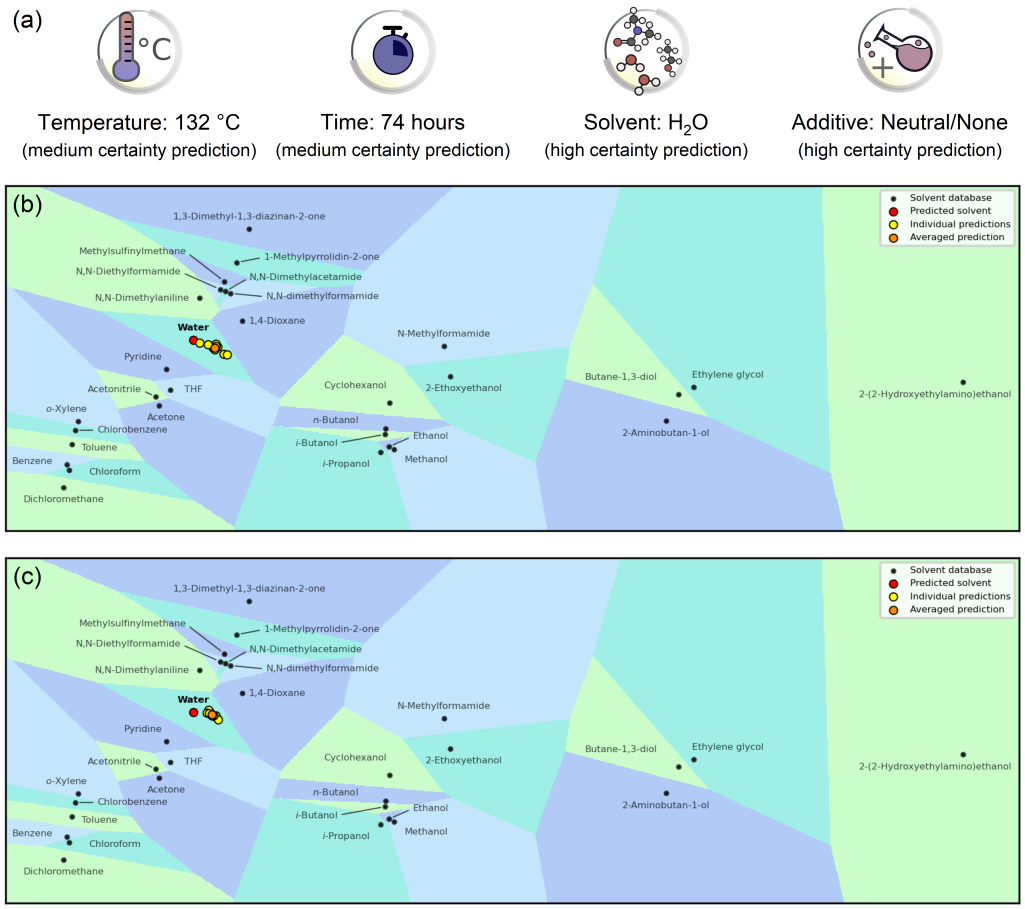

Fig. S1. Machine learning synthesis predictions of 2D altermagnetic MOFs with the MOF Synthesis Prediction Tool.[6] (a) Temperature, reaction time, solvent, and additive predictions for $M(pyz)_2$ (M = Ca and Sr) based on their structures. The certainty of prediction is based on the agreement or disagreement between 10 different models trained on different subsets of the SynMOF dataset. (b, c) 2D visualization of principal component analysis for solvent predictions. The predicted solvent is highlighted in bold. (b) $Ca(pyz)_2$. (c) $Sr(pyz)_2$. The toolkit website: https://mof-synthesis.aimat.science.

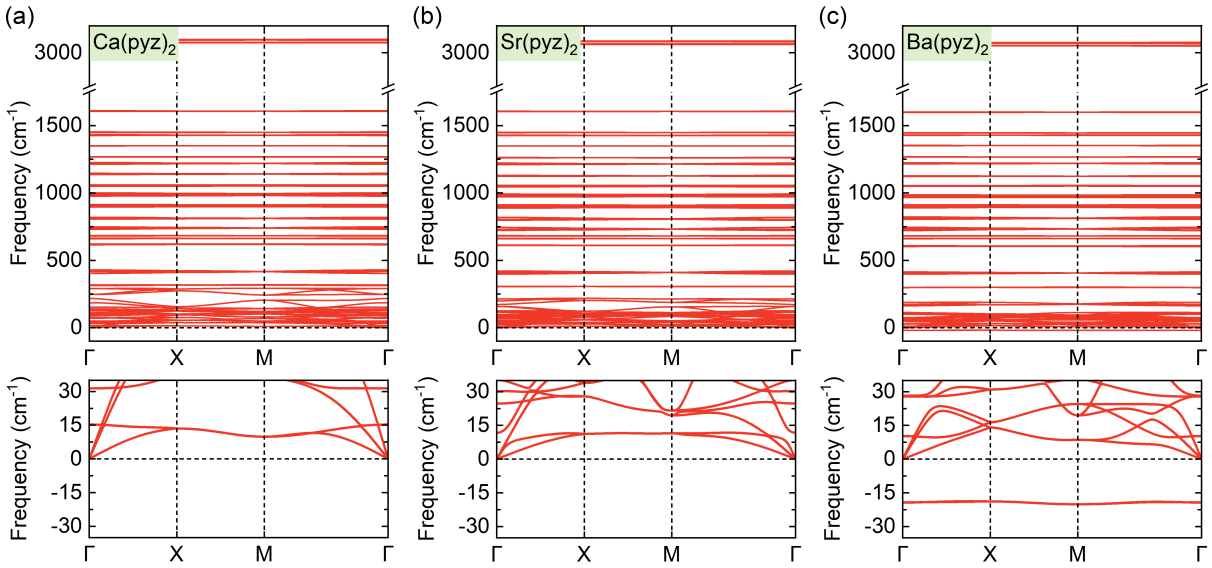

Fig. S2. Phonon band structures representing dynamic stabilities. (a) $Ca(pyz)_2$. (b) $Sr(pyz)_2$. (c) $Ba(pyz)_2$. $Ba(pyz)_2$ is not dynamically stable due to the soft phonon modes at about 20i cm^{-1}, corresponding to the relative vibration of Ba atoms along *c*-axis.

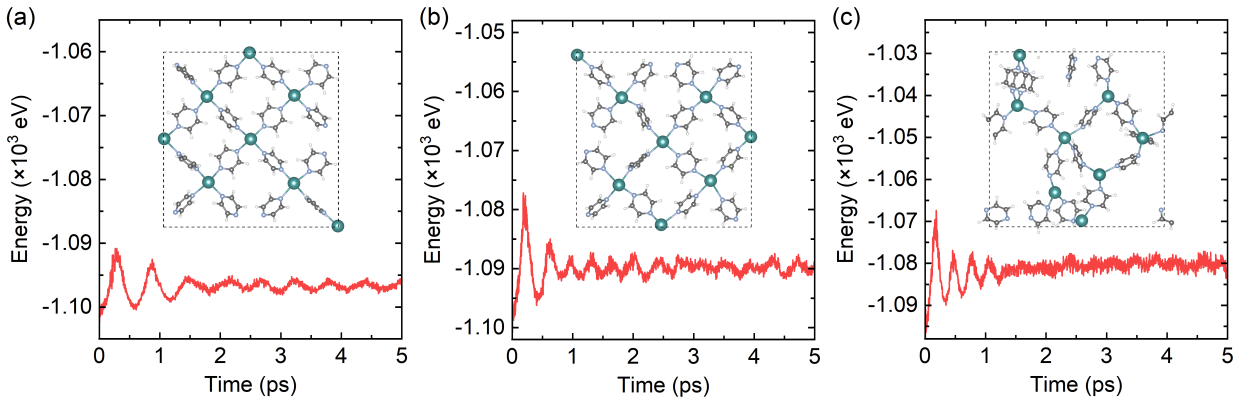

Fig. S3. AIMD simulations representing thermal stabilities of $Ca(pyz)_2$. (a) 300 K. (b) 600 K. (c) 900 K. The illustration in each subfigure represents the structural snapshot of the corresponding temperature at 5 ps. Green, gray, blue, and white balls represent Ca, C, N, and H atoms, respectively.

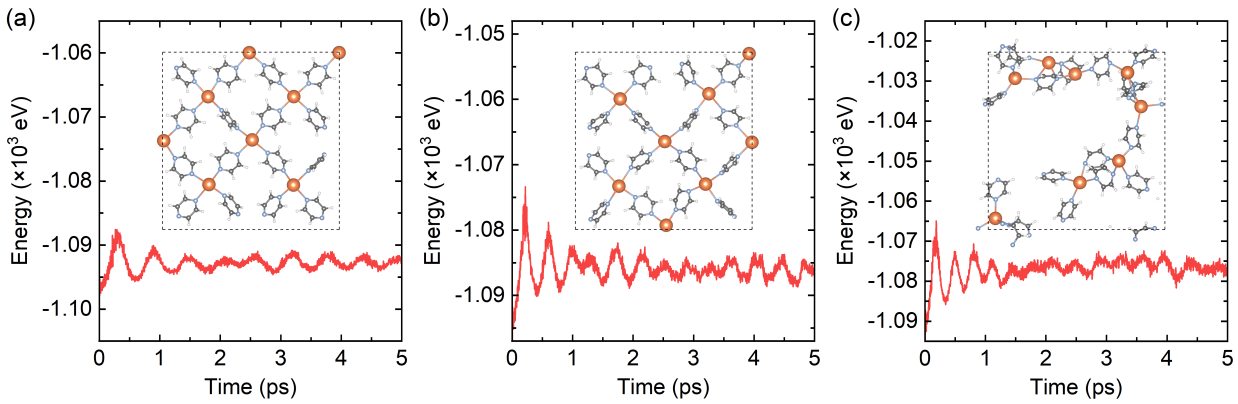

Fig. S4. AIMD simulations representing thermal stabilities of $Sr(pyz)_2$. (a) 300 K. (b) 600 K. (c) 900 K. The illustration in each subfigure represents the structural snapshot of the corresponding temperature at 5 ps. Orange, gray, blue, and white balls represent Sr, C, N, and H atoms, respectively.

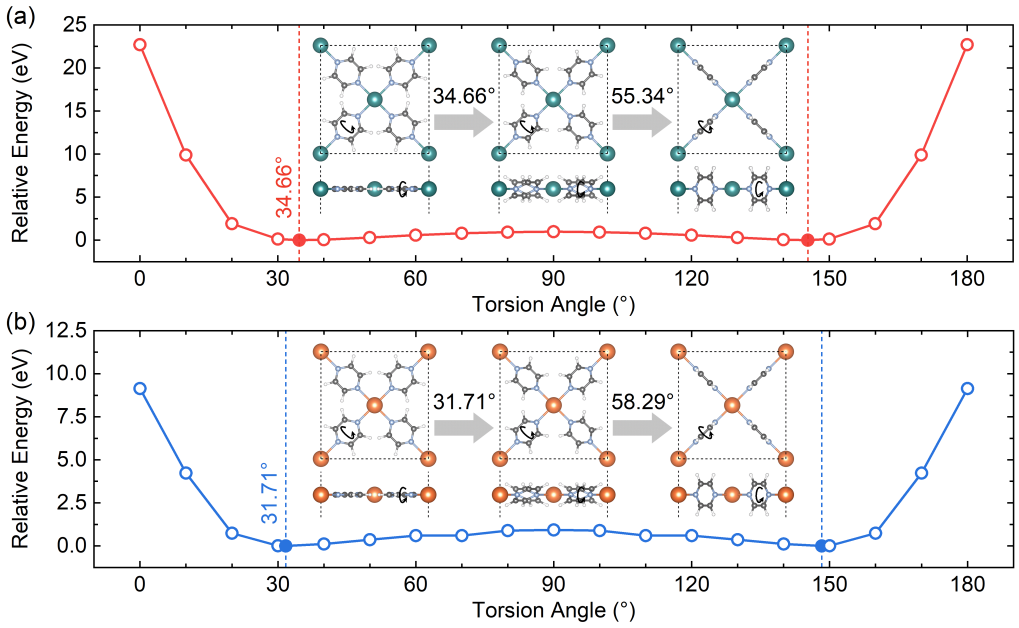

Fig. S5. Relative energies with different torsion angles according to the corresponding most stable structure. (a) $Ca(pyz)_2$. (b) $Sr(pyz)_2$. The self-consistent-field energies with PBE functional and the same lattice scale are investigated with a torsion angle step of 10°, including a flat structure (0° and 180°) and a structure with upright pyrazine ligands (90°, see them in subfigures). The solid dots denote the most stable structure with the relative energy of 0 eV, and the corresponding torsion angle are labeled with dash lines. Green, orange, gray, blue, and white balls represent Ca, Sr, C, N, and H atoms, respectively.

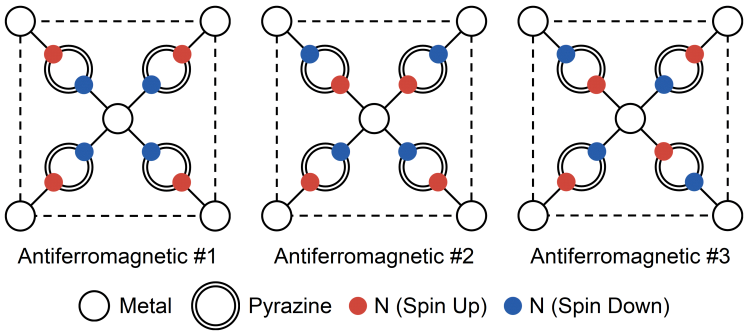

Fig. S6. Spin configurations at N atom level. Three different antiferromagnetic configurations of $Ca(pyz)_2$ and $Sr(pyz)_2$ are considered, where the two N atoms in each pyrazine ligand have opposite spins. The calculated energies and atomic magnetic moments of three antiferromagnetic types are completely consistent with the nonmagnetic type.

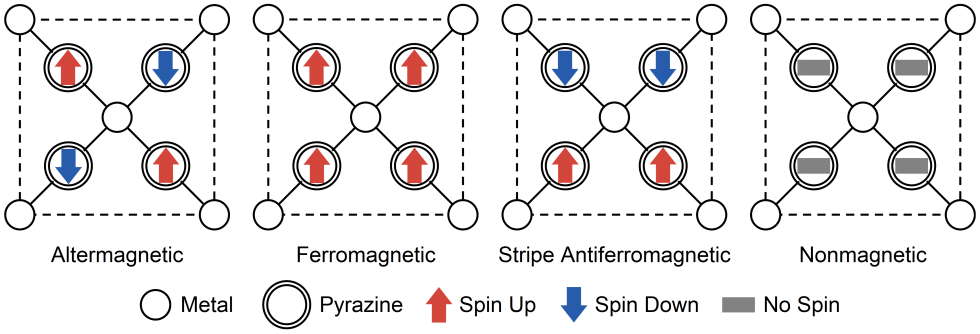

Fig. S7. Spin configurations at pyrazine level. Four different magnetic configurations of $Ca(pyz)_2$ and $Sr(pyz)_2$ based on pyrazine ligands as spin units are considered, where the altermagnetic state is the most stable.

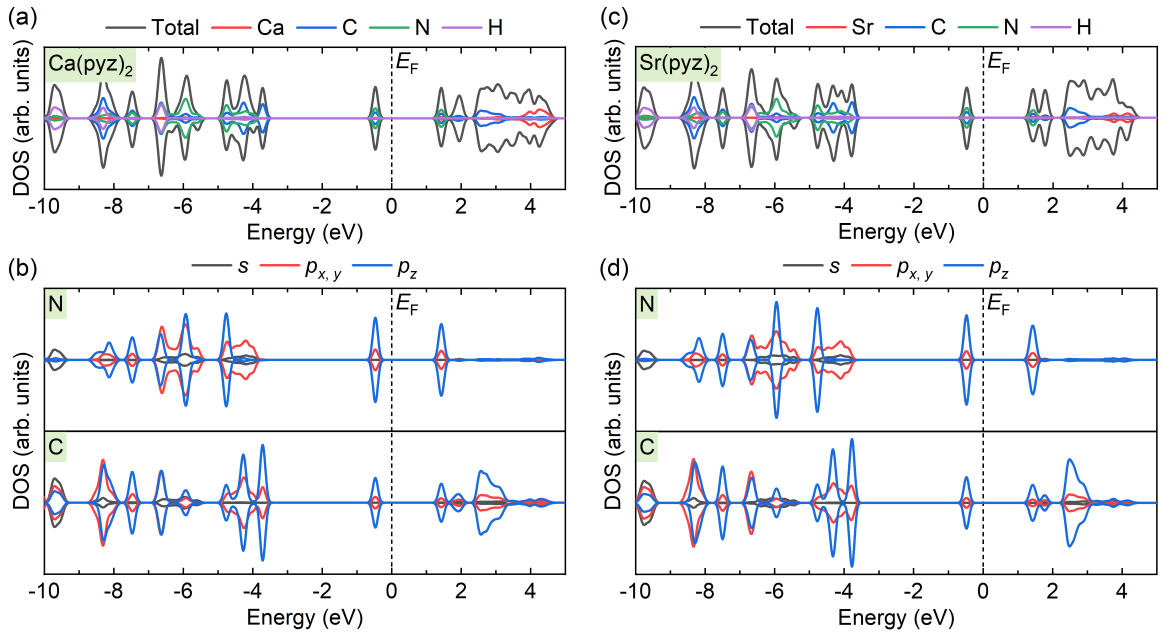

Fig. S8. Density of states (DOS). (a, b) $Ca(pyz)_2$. (c, d) $Sr(pyz)_2$. (a, c) Total and atomically resolved DOS. (b, d) DOS of N projected to s, p_x, p_y, and p_z orbitals. The Fermi level ($\mathcal{E}_F$) is set to 0 eV.

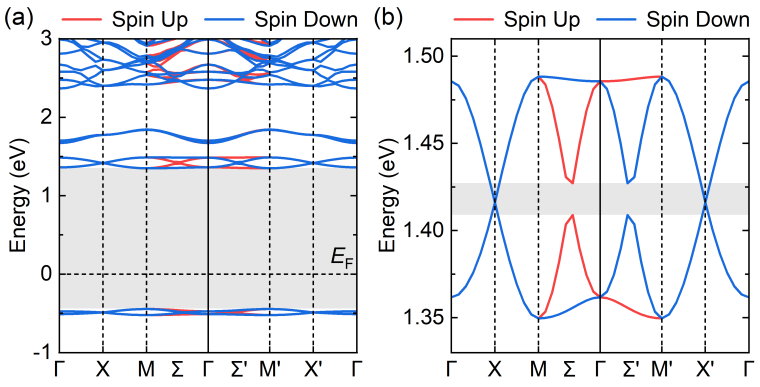

Fig. S9. HSE06 band structure of $Sr(pyz)_2$. (a) The band structure of the altermagnetic 2D $Sr(pyz)_2$ with HSE06 functional passes through the k-path in **Fig. 2d**, with (b) spin-splitting effect around CBM. The gray shadows in (a) and (b) represent the band gap ($\mathcal{E}_g$ = 1.79 eV) and the energy gap (18.22 meV) between the spin-splitting bands near the CBM, respectively. The Fermi level ($\mathcal{E}_F$) is set to 0 eV.

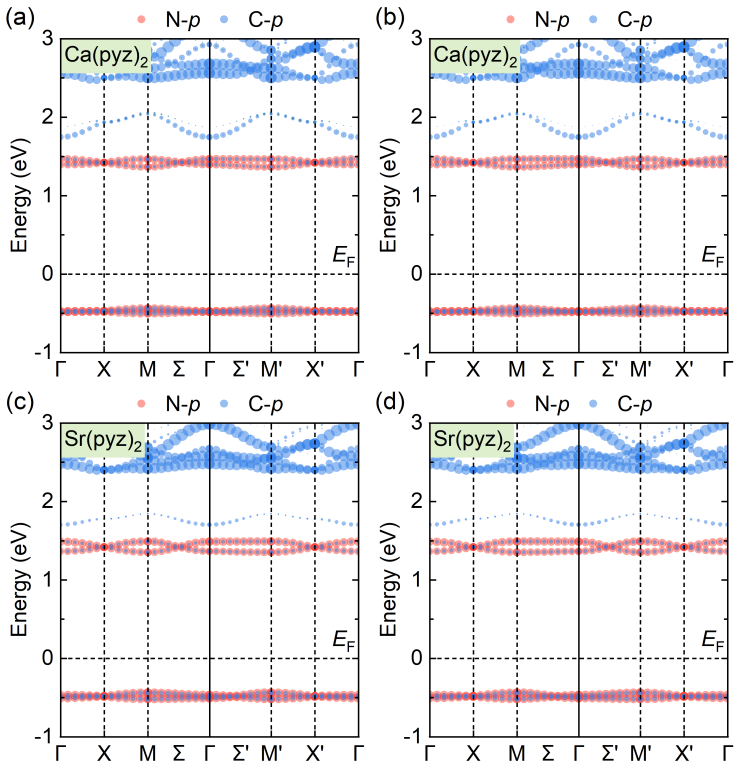

Fig. S10. Orbital-resolved band structure with HSE06 functional. (a, b) $Ca(pyz)_2$. (c, d) $Sr(pyz)_2$. (a, c) Spin up. (b, d) Spin down. The larger the dots, the greater the contribution of corresponding orbitals. The Fermi level ($\mathcal{E}_F$) is set to 0 eV.

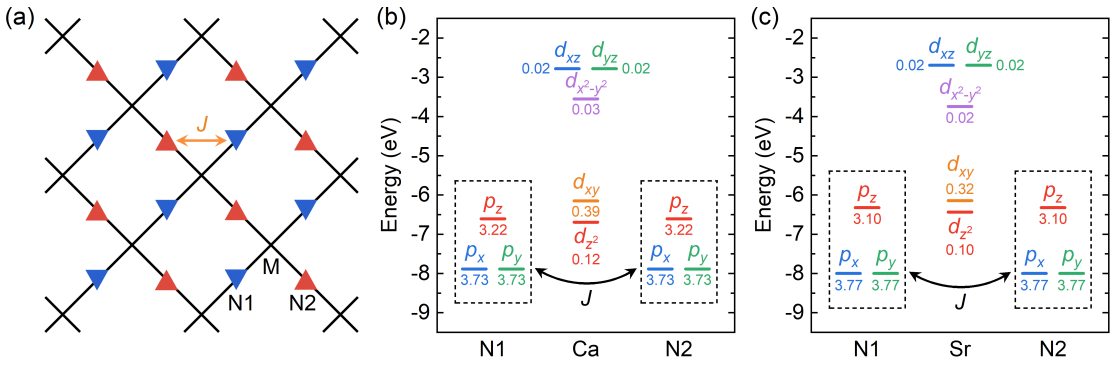

Fig. S11. Altermagnetic exchange. (a) Magnetic pathways. (b, c) Energy levels of metal's *d* orbitals and N's *p* orbitals, where the number of each orbital represents the electron occupation calculated from $\int_{-\infty}^{\mathcal{E}_F} \mathcal{E} \times g(\mathcal{E})d\mathcal{E}$. (b) $Ca(pyz)_2$. (c) $Sr(pyz)_2$. The Fermi level ($\mathcal{E}_F$) is set to 0 eV.

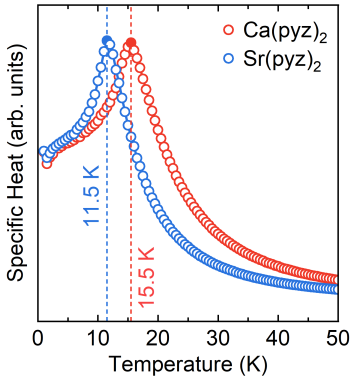

Fig. S12. Altermagnetic transition temperatures. Specific heat is a function of temperature from Monte Carlo simulations based on the HSE06 energies, where the transition temperature is extracted from the peak point of each curve.

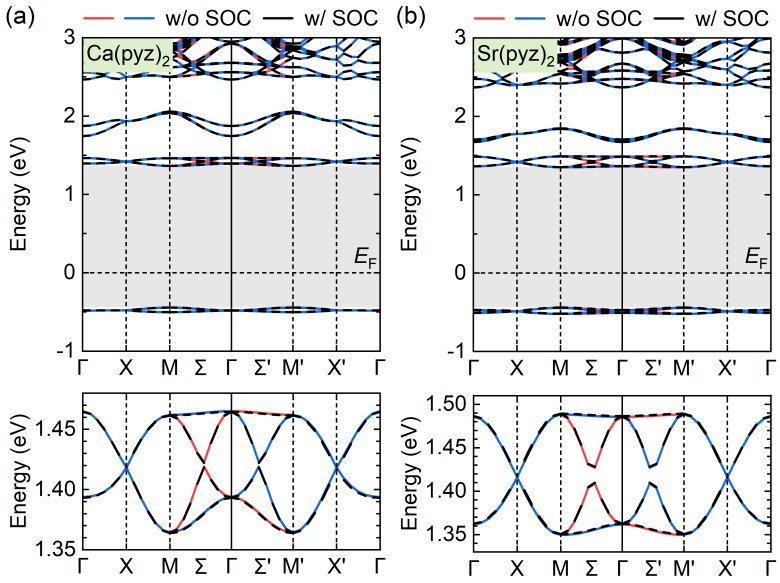

Fig. S13. HSE06 band structures without (red and blue lines) and with (black lines) SOC. (a) $Ca(pyz)_2$. (b) $Sr(pyz)_2$. SOC does not induce weak ferromagnetism and additional spin-splitting. Gray shadows denote band gaps and the Fermi level ($\mathcal{E}_F$) is set to 0 eV.

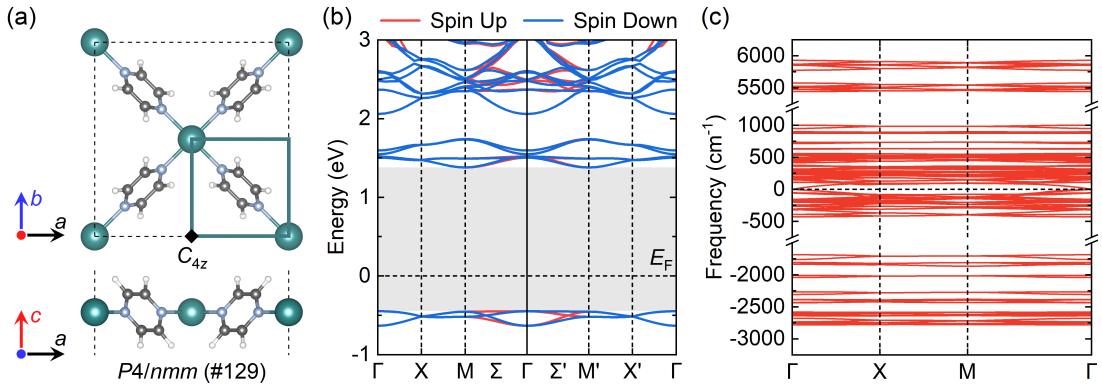

Fig. S14. Structure and dynamic stability of the $P4/nmm$ (#129) $Ca(pyz)_2$. (a) Structure of the $P4/nmm$ (#129) $Ca(pyz)_2$ from the top (top panel) and front (bottom panel) views where the C_{4z} rotation axis is located at the edge center of the tetragonal phase. Green, gray, blue, and white balls represent Ca, C, N, and N atoms, respectively. (b) Band structure of the $P4/nmm$ (#129) $Ca(pyz)_2$ with HSE06 functional *via* the k-path in **Fig. 2d**. The Fermi level ($\mathcal{E}_F$) is set to 0 eV. (c) Phonon band structure of the $P4/nmm$ (#129) $Ca(pyz)_2$ with obvious imaginary frequencies, indicating the $P4/nmm$ (#129) phase is dynamically unstable.

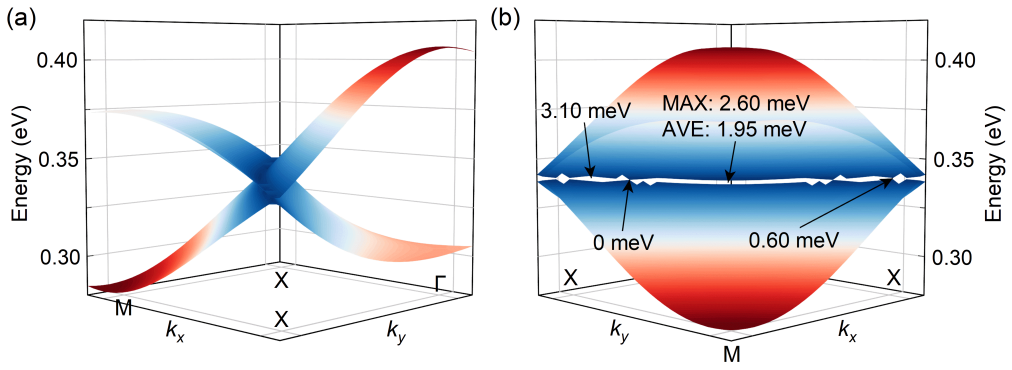

Fig. S15. Σ-centered 3D band structure of $Ca(pyz)_2$. Details of the Σ-centered 3D energy band structure for the altermagnetic spin-splitting around CBM in $Ca(pyz)_2$ with PBE functional are shown from (a) X-X and (b) M-Γ directions. The range of energy gap is labeled in (b).

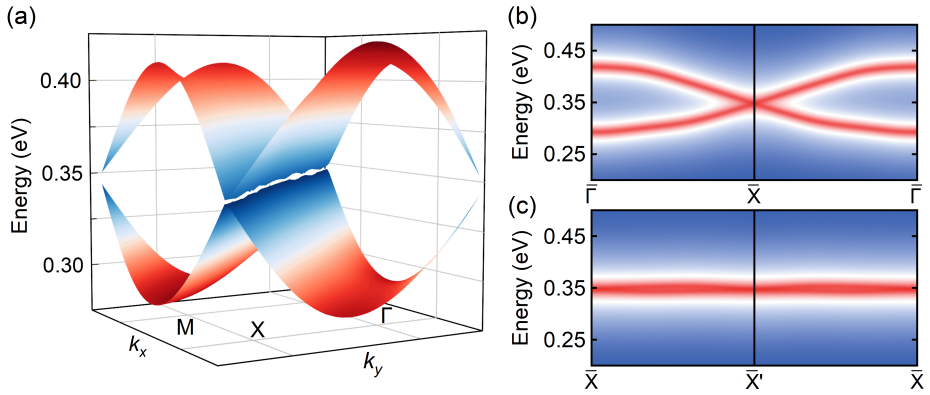

Fig. S16. Topological properties of $Sr(pyz)_2$. (a) Σ-centered 3D band structure of the altermagnetic spin-splitting near CBM for $Sr(pyz)_2$. (b, c) Topological edge states on the (b) (100) and (c) (110) surfaces of BZ for $Sr(pyz)_2$, where the k-points $\overline{\Gamma}$, $\overline{\mathrm{X}}$, and $\overline{\mathrm{X}}'$ are the corresponding projections along the surfaces of BZ. The red color indicates a higher stage along the edge. The topological properties are investigated with PBE functional and the Fermi level ($\mathcal{E}_\mathrm{F}$) is set to 0 eV.

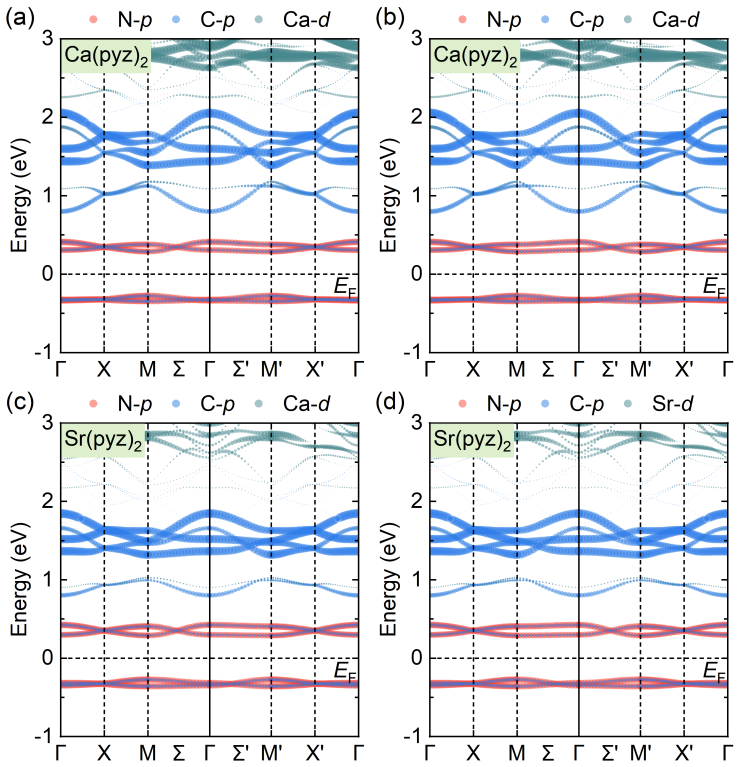

Fig. S17. Orbital-resolved band structure with PBE functional for orbital selection in TBA calculations. (a, b) $Ca(pyz)_2$. (c, d) $Sr(pyz)_2$. (a, c) Spin up. (b, d) Spin down. The larger the dots, the greater the contribution of corresponding orbitals. The Fermi level ($\mathcal{E}_F$) is set to 0 eV.

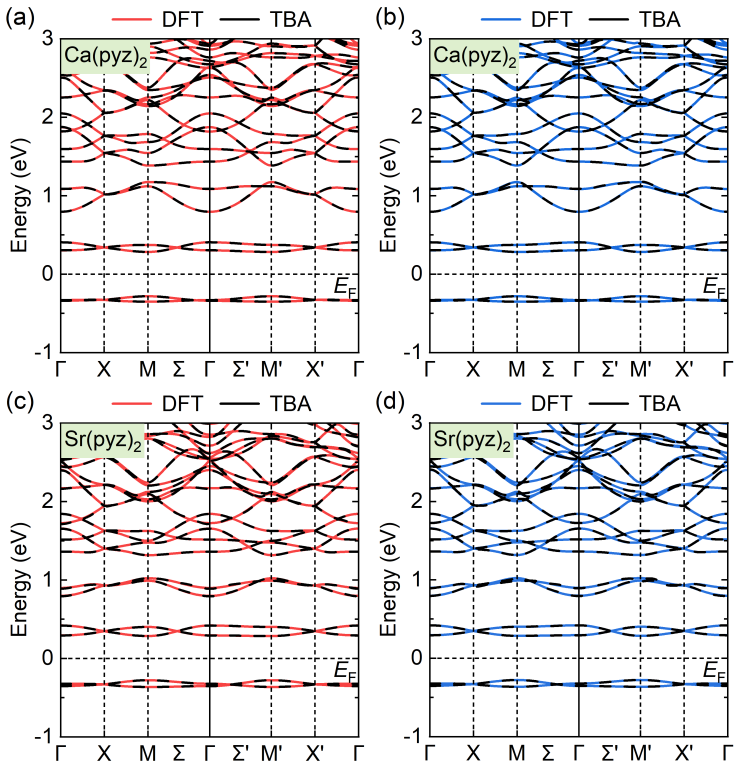

Fig. S18. TBA approximated band structures. (a, b) $Ca(pyz)_2$. (c, d) $Sr(pyz)_2$. (a, c) Spin up. (b, d) Spin down. The calculated band structures based on DFT and TBA of different spins are implemented in VASP and Wannier90, respectively. The PBE functional is adopted in the DFT calculations and the *p* orbitals of N and C are employed to perform the tight-binding Hamiltonian. The Fermi level ($\mathcal{E}_F$) is set to 0 eV.

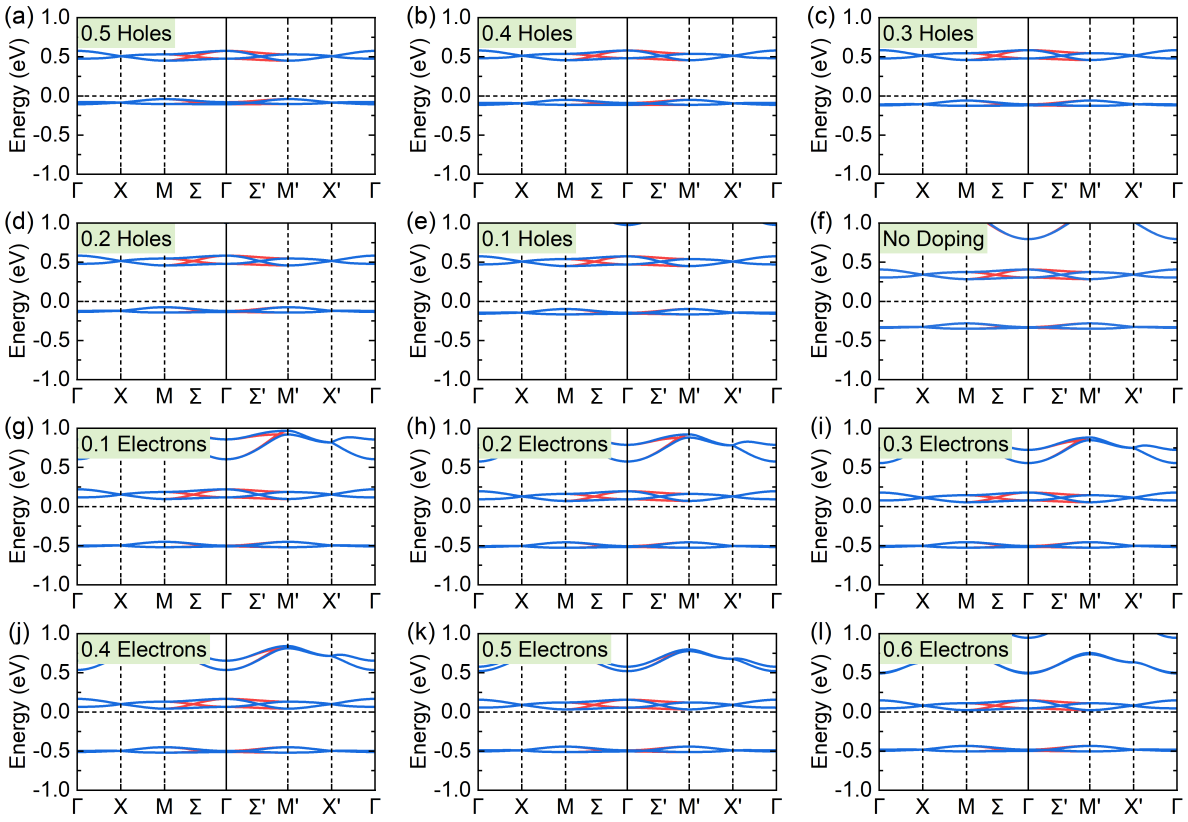

Fig. S19. Band structures around the Fermi level ($\mathcal{E}_F$) when doping with electrons and holes in $Ca(pyz)_2$. (a-e) Doping with holes. (f) No doping. (g-l) Doping with electrons. Band shifts down when the amount of electron in unit cell increases. The Fermi level ($\mathcal{E}_F$) is set to 0 eV.

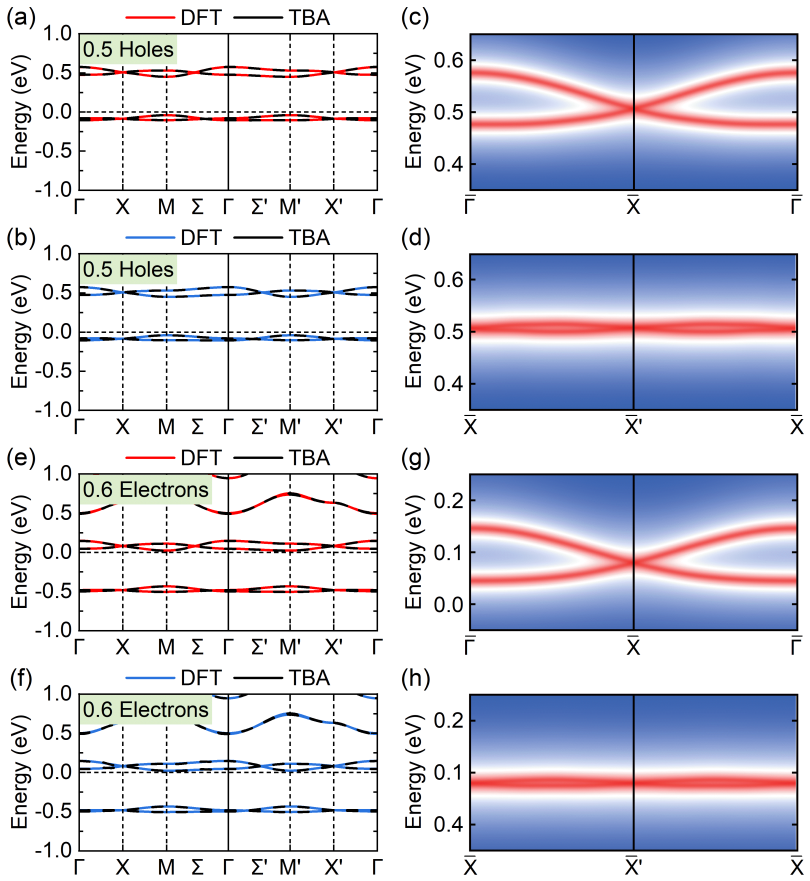

Fig. S20. Topological points and lines when doping with electrons and holes in $Ca(pyz)_2$. (a-d) Doping with 0.5 holes. (e-h) Doping with 0.6 electrons. (a, b, e, f) TBA approximation. (c, d, g, h) Topological edge states on the (c, g) (100) and (d, h) (110) surfaces of BZ. The Fermi level ($\mathcal{E}_F$) is set to 0 eV.

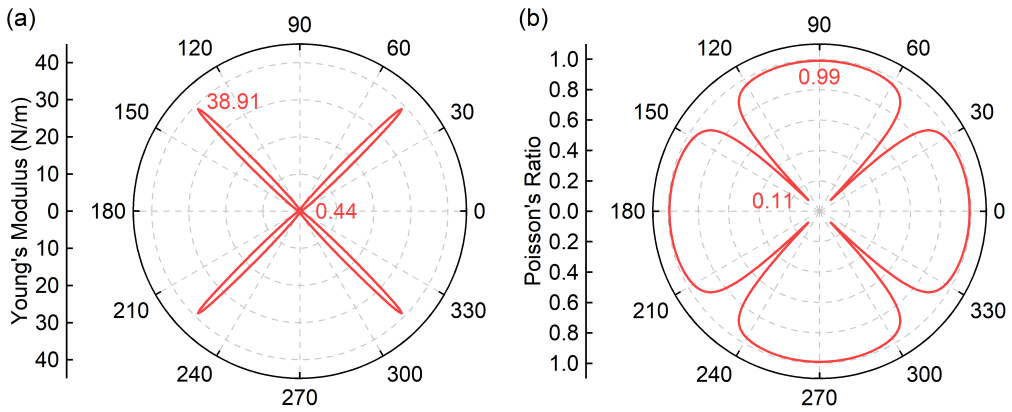

Fig. S21. Mechanical anisotropies of $Ca(pyz)_2$. (a) Young's modulus and (b) Poisson's ratio of the altermagnetic 2D $Ca(pyz)_2$ as a function of the in-plane angle where 0° corresponds to the *a*-axis. The maximum and minimum values are labeled.

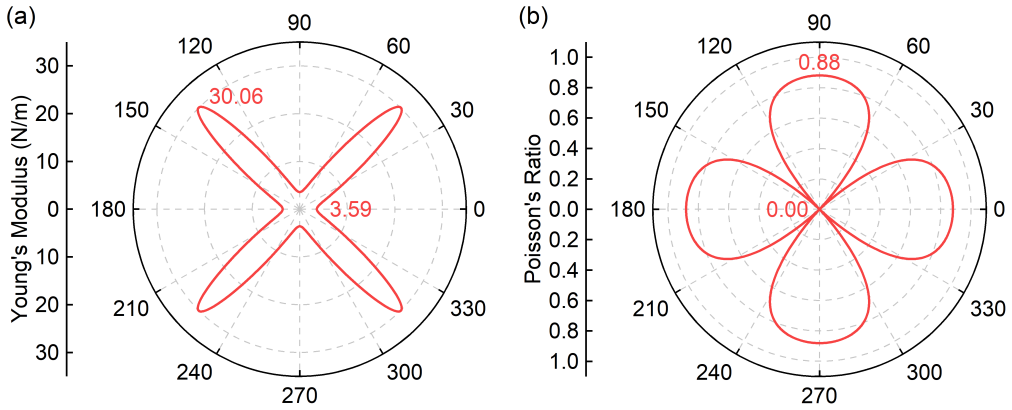

Fig. S22. Mechanical anisotropies of $Sr(pyz)_2$. (a) Young's modulus and (b) Poisson's ratio of the altermagnetic 2D $Sr(pyz)_2$ as a function of the in-plane angle where 0° corresponds to the *a*-axis. The maximum and minimum values are labeled.

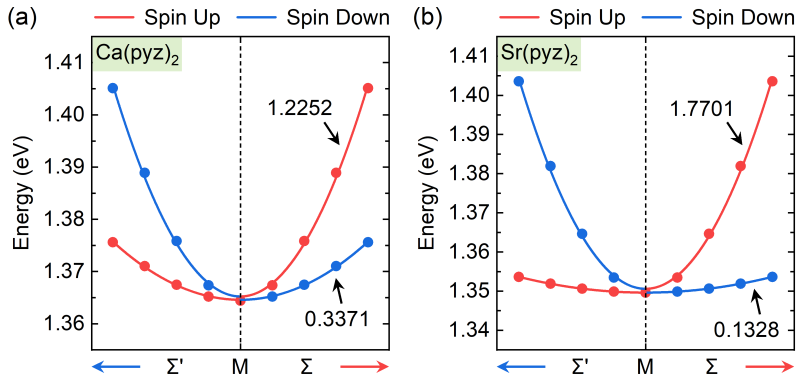

Fig. S23. Electrical anisotropies and effective mass fitting. (a) $Ca(pyz)_2$. (b) $Sr(pyz)_2$. The HSE06 band interpolation of $Ca(pyz)_2$ along Σ′ and Σ directions at CBM starting at M are introduced to fit the effective mass by the quadratic function $y = Ax^2 + Bx + C$, where y and x represent the energy isosurface and k-point coordinate, respectively. The red and blue arrows below the horizontal axis represent the corresponding k-paths as shown in **Fig. 2d**, and the values in the plot are A of each curve for the effective mass calculation as mentioned in **Note S2**.

TABLES

Table S1. Crystallographic details and Wyckoff positions of the $P4/nbm$ (#125) $Ca(pyz)_2$.

Formula	**Space group**	**Unit cell parameters**					
$Ca(C_4H_4N_2)_2$	$P4/nbm$ (#125)	a (Å)	b (Å)	c (Å)	α (°)	β (°)	γ (°)
		10.86	10.86	18.00	90.00	90.00	90.00
Sites	**Wyckoff position**	**Site symmetry**		**Fractional coordinates (x, y, z)**			
C1	16n	1		(0.233105, 0.356114, 0.463150)			
H1	16n	1		(0.057422, 0.282630, 0.433702)			
N1	8j	..2		(0.155685, 0.155685, 0.500000)			
Ca1	2b	422		(0.000000, 0.000000, 0.500000)			

Table S2. Crystallographic details and Wyckoff positions of the $P4/nbm$ (#125) $Sr(pyz)_2$.

Formula	**Space group**	**Unit cell parameters**					
$Sr(C_4H_4N_2)_2$	$P4/nbm$ (#125)	a (Å)	b (Å)	c (Å)	α (°)	β (°)	γ (°)
		11.34	11.34	18.00	90.00	90.00	90.00
Sites	**Wyckoff position**	**Site symmetry**		**Fractional coordinates (x, y, z)**			
C1	16n	1		(0.146323, 0.268180, 0.465939)			
H1	16n	1		(0.061973, 0.285125, 0.438592)			
N1	8j	..2		(0.159504, 0.159504, 0.500000)			
Sr1	2b	422		(0.000000, 0.000000, 0.500000)			

Table S3. Total and local magnetic moments (in μ_B) on each element of $Ca(pyz)_2$ in different magnetic states with HSE06 functional. The "+" and "−" symbols represent the up and down spins corresponding to the red and blue colors in **Fig. S5**, respectively. The bold column represents the magnetic ground state and its magnetic moments. "AFM" in the fourth column is the abbreviation for "antiferromagnetic".

	Altermagnetic	**Ferromagnetic**	**Stripe AFM**	**Nonmagnetic**
μ_{Ca}	**0.000**	0.000	0.000	0.000
μ_C	**+0.030 −0.030**	0.030	+0.030 −0.030	0.000
μ_N	**+0.232 −0.232**	0.233	+0.233 −0.233	0.000
μ_H	**+0.001 −0.001**	−0.001	+0.001 −0.001	0.000
μ_{total}	**0.000**	4.000	0.000	0.000

Table S4. Total and local magnetic moments (in μ_B) on each element of $Sr(pyz)_2$ in different magnetic states with HSE06 functional. The "+" and "−" symbols represent the up and down spins corresponding to the red and blue colors in **Fig. S5**, respectively. The bold column represents the magnetic ground state and its magnetic moments. "AFM" in the fourth column is the abbreviation for "antiferromagnetic".

	Altermagnetic	**Ferromagnetic**	**Stripe AFM**	**Nonmagnetic**
μ_{Sr}	**0.000**	0.016	0.000	0.000
μ_C	**+0.029 −0.029**	0.029	+0.030 −0.030	0.000
μ_N	**+0.234 −0.234**	0.235	+0.235 −0.235	0.000
μ_H	**+0.001 −0.001**	−0.001	+0.001 −0.001	0.000
μ_{total}	**0.000**	4.000	0.000	0.000

Table S5. Crystallographic details and Wyckoff positions of the $P4/nmm$ (#129) $Ca(pyz)_2$.

Formula	**Space group**	**Unit cell parameters**					
$Ca(C_4H_4N_2)_2$	$P4/nmm$ (#129)	a (Å)	b (Å)	c (Å)	α (°)	β (°)	γ (°)
		10.86	10.86	18.00	90.00	90.00	90.00
Sites	**Wyckoff position**	**Site symmetry**		**Fractional coordinates (x, y, z)**			
C1	16k	1		(0.329905, 0.259314, 0.443692)			
H1	16k	1		(0.394182, 0.264434, 0.397075)			
N1	8h	..2		(0.344515, 0.344515, 0.500000)			
Ca1	2b	$\bar{4}m2$		(0.000000, 0.000000, 0.500000)			

Table S6. Relative energy differences (in meV per unit cell) of $Ca(pyz)_2$ according to the altermagnetic phase when doping electrons (positive doping values) and holes (negative doping values) with PBE functional. The altermagnetic ground state can be maintained within a doping range of up to 0.5 holes or 0.6 electrons. Bold values denote their corresponding magnetic ground states.

Doping	Altermagnetic	Ferromagnetic	Stripe AFM	Nonmagnetic
−0.7	0.00	−2.38	**−3.38**	216.35
−0.6	0.00	2.27	**−0.59**	234.42
−0.5	**0.00**	7.43	3.75	252.61
−0.4	**0.00**	15.71	4.17	271.31
−0.3	**0.00**	17.30	4.14	287.75
−0.2	**0.00**	23.53	7.66	308.09
−0.1	**0.00**	30.62	11.38	325.64
0.0	**0.00**	40.26	16.63	340.20
0.1	**0.00**	33.84	13.15	325.02
0.2	**0.00**	28.64	10.29	305.89
0.3	**0.00**	23.05	7.45	287.48
0.4	**0.00**	18.88	5.16	267.74
0.5	**0.00**	13.26	2.00	251.38
0.6	**0.00**	10.35	3.50	230.33
0.7	0.00	6.77	**−4.03**	215.91
0.8	0.00	3.66	**−1.83**	198.02

Table S7. Relative energies (in μeV per unit cell) of different magnetization directions and easy axes (EA).

	[100]	**[010]**	**[110]**	**[001]**	**EA**
$Ca(pyz)_2$	0.21	0.21	0.32	0.00	Out-of-plane
$Sr(pyz)_2$	0.95	0.95	0.99	0.00	Out-of-plane

REFERENCES

1 D. B. Litvin and W. Opechowski, *Physica*, 1974, **76**, 538–554.
2 D. B. Litvin, *Acta Cryst. A*, 1977, **33**, 279–287.
3 L. Šmejkal, J. Sinova and T. Jungwirth, *Phys. Rev. X*, 2022, **12**, 031042.
4 H. Ma, M. Hu, N. Li, J. Liu, W. Yao, J. Jia and J. Liu, *Nat. Commun.*, 2021, **12**, 2846.
5 J. Qiao, J. Zhou, Z. Yuan and W. Zhao, *Phys. Rev. B*, 2018, **98**, 214402.
6 Y. Luo, S. Bag, O. Zaremba, A. Cierpka, J. Andreo, S. Wuttke, P. Friederich and M. Tsotsalas, *Angew. Chem. Int. Ed.*, 2022, **61**, e202200242.